Petroleum 1 (2015) 173–186

Contents lists available at ScienceDirect

Petroleum

journal homepage: www.keaipublishing.com/en/journals/petlm

Original article

# Characterization of the pore system in an over-mature marine shale reservoir: A case study of a successful shale gas well in Southern Sichuan Basin, China

Yang Yang [a], Kunyu Wu [a, b, *], Tingshan Zhang [a], Mei Xue [c]

[a] State Key Laboratory of Oil and Gas Reservoir Geology and Exploitation, Southwest Petroleum University, Chengdu 610059, PR China
[b] Research Institute of Exploration and Development of Qinghai Oil Field Company, CNPC, Dunhuang 736202, PR China
[c] Institute of Petroleum Geology and Exploitation, 1st Oil Production Plant of Qinghai Oil Field Company, CNPC, Mangya 816400, PR China

ARTICLE INFO

*Article history:*
Received 16 July 2015
Accepted 23 July 2015

*Keywords:*
Pore system
SEM imaging
Mercury injection porosimetry
Low-pressure nitrogen adsorption
Wufeng–Longmaxi gas shale

ABSTRACT

During the past two years the shale gas exploration in Southern Sichuan basin received some exciting achievements. Data of a new appraisal well showed that the gas producrtions of vertical well and horizontal well are ~1.5 × $10^4$ $m^3$/day/well (with maximum ~3.5 × $10^4$ $m^3$/day/well) and ~12.5 × $10^4$ $m^3$/day/well (with maximum ~40 × $10^4$ $m^3$/day/well), respectively, indicating a good gas potential in this area. Eight core samples from the reservoir were investigated by using a carbon sulfur analyzer, microphotometry, x-ray diffractometry, field-emission scanning electron microscopy (FE-SEM), mercury injection porosimetry (MIP), and low-pressure nitrogen adsorption to obtain a better understanding of the reservoir characteristics of the Upper Ordovician–Lower Silurian organic-rich shale. Results show that the total organic carbon (TOC) content ranges from 0.5% to 5.9%, whereas the equivalent vitrinite reflectance (*VRr*) is between 2.8% and 3.0%. Pores in the studied samples were observed in three modes of occurrence, namely, interparticle pores, intraparticle pores, and intraparticle organic pores. The total porosity (*P*) ranges from 1.6% to 5.3%, and MIP data sets suggest that pores with throats larger than 20 nm contribute little to the pore volume. Low-pressure $N_2$ adsorption isotherms indicate that the total specific surface area ($S_{BET}$) ranges from 9.6 $m^2$/g to 18.9 $m^2$/g, and the pore volume (*V*) ranges from 0.011 $cm^3$/g to 0.020 $cm^3$/g. The plot of $dV/dW$ versus *W* shows that the fine mesopores (pore $size_{(BJH)}$ < 4 nm) mainly contribute to the pore volume. The *P*, $S_{BET}$, and *V* show a good positive correlation with TOC and a weak positive correlation with the total clay mineral content, thus indicating that the nanopores are mainly generated by the decomposition of organic matter. The reservoir characteristics of the Upper Ordovician–Lower Silurian organic-rich shale are comparable with commercial shale gas plays in North America. The sample gas contents with TOC >2% are more than 3.0 $m^3$/ton. The observation can be a good reference for the future exploration and evaluation of reservoir in this area.



## 1. Introduction

The successes of North American commercial shale gas development has attracted attention worldwide and has resulted in renewed research interest on argillaceous rocks in the past few years [1,2]. A thorough understanding of the pore systems of gas shale reservoirs can help us to better understand gas storage and transport mechanisms in practice. However, the pore systems of unconventional natural gas reservoirs are difficult to characterize because of the extremely small pore sizes and their

* Corresponding author. State Key Laboratory of Oil and Gas Reservoir Geology and Exploitation, Southwest Petroleum University, Chengdu 610059, P. R. China.
*E-mail address:* wukunyu1986@126.com (K. Wu).
Peer review under responsibility of Southwest Petroleum University.

Production and Hosting by Elsevier on behalf of KeAi

http://dx.doi.org/10.1016/j.petlm.2015.07.011

generally wide distribution [3,4]. Pore distribution ranges from microscopic to macroscopic in almost all gas shale reservoirs [1,3-5]. These pores are usually called macropores (i.e., widths exceeding about 50 nm), mesopores (i.e., widths between 2 nm and 50 nm), and micropores (i.e., widths not exceeding about 2 nm) [6]. Given that conventional methods for characterizing the pore systems of gas shale reservoirs are limited, hybrid techniques such as fluid invasion and radiation methods are typically applied to measure the full pore size and distribution [3,4]. Mercury porosimetry is the most widely used characterization technique for conventional reservoirs and can investigate pore throats between 500 μm and 3.5 nm [7]. However, mercury porosimetry cannot completely characterize the pore structure of unconventional reservoirs; thus, other techniques, such as gas adsorption, have been applied to study fine-grained reservoirs that contain micropores [3-5,8-13]. Radiation methods have also progressed during the past decades, thus facilitating the direct investigation pore shapes and structures in unconventional reservoirs. Several types of microscopic imaging technologies (radiation methods), such as scanning electron microscopy (SEM) [1,5,13-17], small-angle and ultra-small-angle neutron scattering [4], and X-ray CT [18], have been successfully applied to characterize the pore system of unconventional shale reservoirs. Studies of gas shale reservoirs demonstrate that a combination of fluid invasion and radiation methods can be used to study the pore system characteristics of reservoirs from micro-to macro-scales [4]. Such studies will help us to more thoroughly understand the gas potential, transportation mechanisms, and accumulation mechanisms of gas shale reservoirs.

Unlike the long time systemic studies on pore systems of gas shale reservoirs in North America, studies on pore systems of gas shale reservoirs in China have received attention until very recently. The Lower Cambrian (Qiongzhusi formation and its equivalents) and Upper Ordovician to Lower Silurian (Wufeng–Longmaxi formation and their equivalents) marine shales in south China are considered to have the highest potential as shale gas strata. Both the Lower Cambrian and the Upper Ordovician to Lower Silurian shale sets have high thermal maturity, their equivalent vitrinite reflectance (*VRr*) ranges from 2.3% to 5.2% and from 1.6% to more than 3.6%, respectively [19]. The Mississippian Barnett shale gas play indicates that organic-rich marine black shale with high maturity usually has high potential for high gas content and flow rates [20]. In addition, the quartz and carbonate contents of the Lower Paleozoic marine shales in south China are similar to those of the Mississippian Barnett shale [21]. Therefore, national marine shale gas exploration and production demonstration areas have been established in southern China. However, the complex postgeneration tectonic motions (e.g. compression and strike-slip) make the gas exploration and production in marine shales in China faces higher risks than in North America [21]. Exploration practices in the past few years demonstrate that the over-mature organic-rich shales in south China are strongly heterogeneous, and the resource potential of some areas is not as significant as predicted in the past. To improve the exploration success rate, geologists have focused on the mechanisms of shale gas accumulation in China. The pore system in a gas shale reservoir as an important control factor on shale gas accumulation and hence were studied, in the past a few years, many reports about the pore system in Longmaxi organic-rich shales were published [13,22-24]. Whereas, most of them were focused on the wells outside the Sichuan Basin [13,23,24], where the production tests showed that shale gas potential is not as significant as predicted before. This study focuses on the pore system and reservoir characteristics of organic-rich marine shale cores from a successful shale gas appraisal well, these data can be helpful for understanding the characteristics of over-mature marine shale reservoirs and can provide a good reference for the future exploration.

## 2. Geological setting and core description

The Sichuan Basin is located on the northwestern Yangtze Plate (Fig. 1a) and is the remnant of the originally Lower Paleozoic Upper Yangtze cratonic basin [25,26]. The Wufeng–Longmaxi formations were formed during the Late Ordovician and Early Silurian Periods (Katian to Aeronian; 447–438 Ma [27]; www.stratigraphy.org/index.php/ics-chart-timescale). Paleontological and paleoclimatic data indicate that the South China Block was located in the tropical zone during the Late Ordovician to Early Silurian Periods and formed the continental shelf sea of the Upper Yangtze Plate [28]. Due to the widespread glaciations that began at the Katian–Hirnantian boundary [29,30], the Yangtze Craton experienced widespread regression in the Late Ordovician, thus blocking the sea water circulation and causing the entire Yangtze Shelf Sea to become stagnant [26]. The glaciers began to melt and a global-scale transgression occurred at the beginning of the Silurian Period. However, the stagnant sedimentary environment on the Yangtze Plate did not change in the early Rhuddanian (i.e., 443.4 Ma–440.8 Ma), thus creating favorable conditions for organic matter preservation. Black shale and black siliceous shale sets formed the predominant lithofacies of the Wufeng formation and lower sections of the Longmaxi formation [26]. The Wufeng–Longmaxi organic-rich shales have been interpreted as important source rock sets within and around the Sichuan Basin [19]. Their depositional centers were located in the southern and eastern parts of the Sichuan Basin, and the thickness of the strata varies from several meters to more than 100 m. However, the Wufeng–Longmaxi black shales are absent in the northwestern Sichuan Basin (Fig. 1b). The total organic carbon (TOC) content of the Wufeng–Longmaxi organic-rich shales ranges from ~0.5% to ~6%, and the kerogen of the organic matter is dominated by Types I and II with *VRr* values in the range of 1.6%–3.6%, thus indicating promising shale gas prospects [13,19]. During the past a few years, exploration works within and around the Sichuan Basin have been conducted by PetroChina, Shell, and Sinopec etc. Some appraisal wells have shown encouraging gas shows, thus indicating promising shale gas potential in this area [31,32].

This study used an appraisal well of good gas production that was drilled recently to evaluate the Wufeng–Longmaxi black shales. The well was located on the southern margin of the Sichuan Basin (Fig. 1b). The Longmaxi formation was subdivided into two members: the predominant lithofacies of the upper member is silty limestone, and the lower one was mostly black shale. The main lithofacies of the Wufeng formation in this region is black limy shale (Fig. 1c). Graptolite fossils are abundant in the Wufeng–Longmaxi black shales, thus indicating that the sedimentary environment of the rocks was anoxic to suboxic [33].

## 3. Sampling and analytical methods

Eight core shale samples were collected from the well in the interval between 2473 m and 2513 m. The TOC, vitrinite reflectance, and mineral composition of the black shales were measured by using an infrared carbon sulfur analyzer, microphotometry, and x-ray diffractometry (XRD) to characterize their petrology and mineralogy. The pore system of the gas shale reservoir was studied by using field-emission scanning

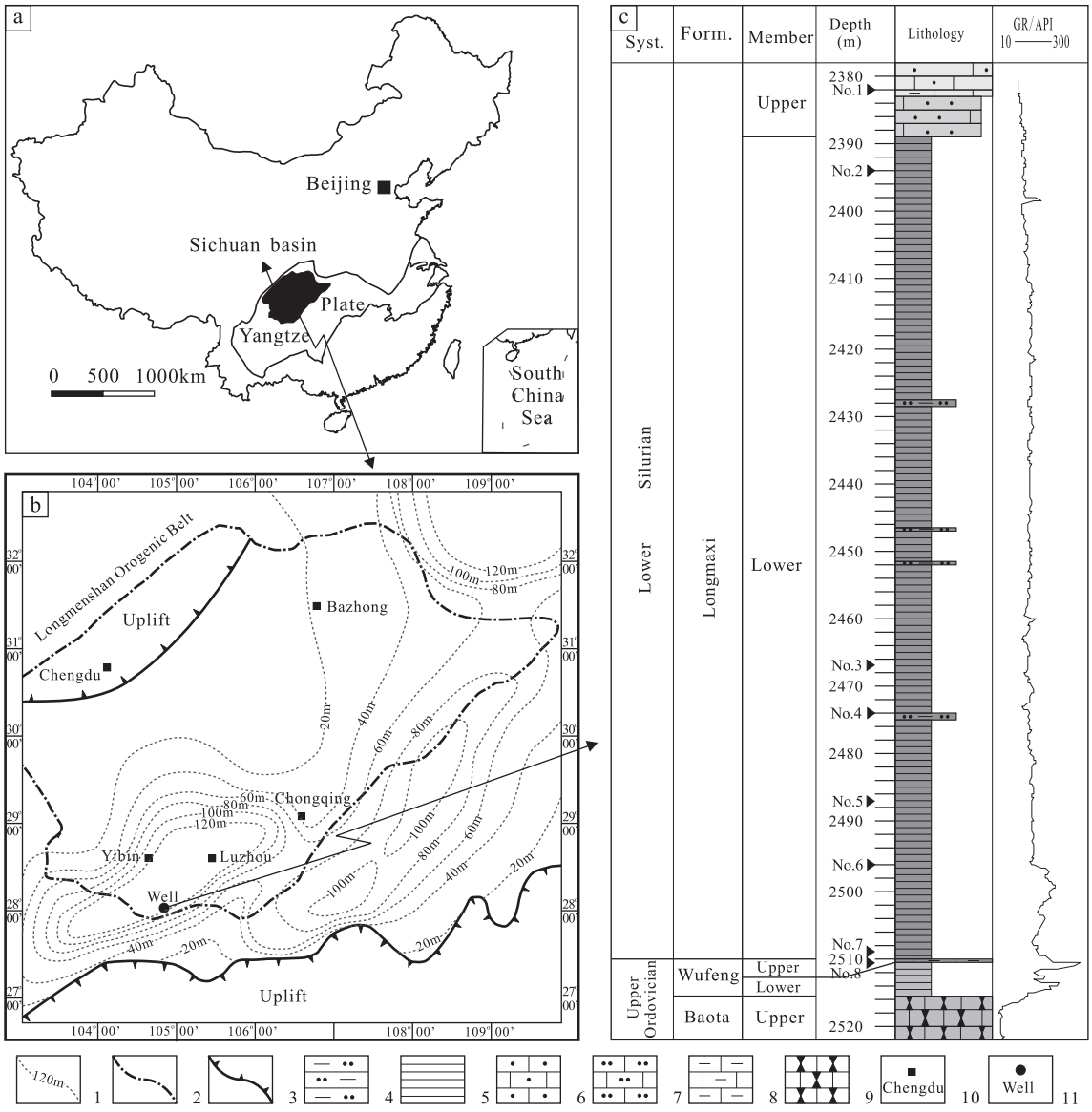


**Fig. 1.** General tectonic setting, strata thickness contours, and lithological column of the Wufeng–Longmaxi formations. a) Tectonic location of the Sichuan Basin (modified according to Ref. [50]; b) strata distribution and thickness contours of the Wufeng–Longmaxi formation (modified according to Refs. [31,33,51]; c) general lithological column of the Wufeng–Longmaxi formations; 1) thickness contours of the Wufeng–Longmaxi formation; 2) boundary of the Sichuan Basin; 3) pinch-out line of the Wufeng–Longmaxi formations; 4) silty mud-stone; 5) black shale; 6) sandy limestone; 7) silty limestone; 8) argillaceous limestone; 9) nodular limestone; 10) town; 11) well location. Solid triangles are sampling locations.

electronic microscopy (FE-SEM), mercury injection porosimetry (MIP), and low-pressure nitrogen gas adsorption.

The TOC was measured with a LECO CS-400 carbon sulfur analyzer (combustion at temperatures over 800 °C). To remove the carbonate the samples were treated with hydrochloric acid (1:1) before analysis.

Given the marine carbonate and pre-Devonian source rocks commonly do not contain vitrinite, but may have a significant amount of solid bitumen associated with generated hydrocarbons [34], hence solid bitumen reflectance (BRr) was measured as the thermal maturity indicator. All measurements were performed on polished blocks under reflected light by using a CRAIC QDI 302 microscope spectrophotometer system. The percentage random reflectance was measured using a 40 × / 0.85 lens in oil immersion (n = 1.518) at a wavelength of 546 nm. The BRr was converted to VRr by using the equation suggested by Ref. [37]:

$$VRr = (BRr + 0.2443)/1.0495. \quad (1)$$

Mineral composition of crushed core shale samples was determined by using an X' Pert Pro x-ray diffractometer with a Cu anode at 40 kV, 20 mA, and 0.154 nm wavelength.

The pore morphology was investigated using a QuantaTM 250 FE-SEM at high vacuum. The surfaces of samples were milled by argon ions and then coated with gold.

Total porosity testing was conducted following the procedure of [35]. The sample porosity was calculated by subtracting the skeletal density from the bulk density. Mercury immersion and Archimedes' Principle of Displacement were used to determine the sample bulk density. Skeletal density was obtained by helium pycnometry.

Given the broad PSD in the gas shale reservoir, MIP with Quantachrome PoreMaster 60 was used to determine the pore-

throat distribution of shales. The capillary diameter was calculated by using the equation of Washburn [36]:

$$p = \frac{-4\gamma \cos\theta}{d} \tag{2}$$

where $p$ is the pressure, $\gamma$ is the surface tension of the liquid, $\theta$ is the liquid contact angle, and $d$ is the diameter of the capillary.

Low-pressure nitrogen adsorption measurements were conducted on a QUADRASORB SI Surface Area and Pore Size Analyzer (Quantachrome, U.S.) at −195.8 °C. The determination of the adsorption isotherms was accordance with [37]; the crushed samples (60–80 mesh size, ~250–180 μm) were dried and degassed at temperature of ~110 °C in a high vacuum apparatus (~10 mPa) for over 12 h. The purity of nitrogen used as the adsorptive is higher than 99.9%. To investigate the hysteresis types, both adsorption and desorption isotherms were measured. The relative pressure ($p/p_o$) intervals were accordance with [8]; ranging from 0.075 to 1.

To calculate the specific surface areas ($S_{BET}$), the linear form equation of Brunauer–Emmett–Teller (BET) was applied:

$$\frac{p}{V_{ads}(p_o - p)} = \frac{1}{V_m \cdot C_{BET}} + \frac{C_{BET} - 1}{V_m \cdot C_{BET}} \times \frac{p}{p_o}, \tag{3}$$

where $p_o$ is the saturation pressure of pure nitrogen, $V_{ads}$ is the adsorbed volume at the relative pressure $p/p_o$, $V_m$ is the monolayer volume, and $C_{BET}$ is a constant, which is related exponentially to the enthalpy of adsorption in the first adsorbed layer [37].

We used specific criteria rather than the same relative pressure range for all materials to select the relative pressure range and objectively determine the fitting range of the BET plot. These criteria were as follows: (1) the resulting parameter $C_{BET}$ and intercept on the ordinate of the BET-plot should both be positive; (2) the term $V_{ads}(p_o - p)$ should continuously increase together with $p/p_o$, if not the pressure range should be narrowed [38]. $S_{BET}$ was calculated by using the following equation:

$$S_{BET} = \frac{0.001 \times V_m}{22.4} \times N \times A_{N_2}, \tag{4}$$

where $V_m$ is the monolayer volume in $cm^3/g$, $N$ is the Avogadro number, and $A_{N2}$ is the atomic surface area of $N_2$ (0.162 $nm^2$ at −195.8 °C, [37].

PSD was calculated by using the Barrett–Joyner–Halenda (BJH) model, which can predict that the condensation of nitrogen in a pore with radius $r$ occurs at a pressure provided by the following modified Kelvin equation:

$$\ln(p/p_o) = -\frac{\alpha\gamma_N V_m}{RT(r - t)}, \tag{5}$$

where $\gamma_N$ is the surface tension of liquid nitrogen, $V_m$ is the molar volume of liquid nitrogen, $R$ is the gas constant; $T$ is the temperature (−195.8 °C), $\alpha$ is a factor that accounts for the shape of the gas/liquid interface. $t$ was calculated using the following empirical equation [39]:

$$\log(p/p_o) = 0.034 - \frac{13.99}{t^2}, \tag{6}$$

## 4. Results

### 4.1. Petrology and mineralogy

Organic-rich black shale (Fig. 2a) is the predominant lithofacies of the Wufeng–Longmaxi gas shale reservoir. Quartz, aluminosilicate (e.g., albite) and clay minerals, and carbonate minerals form the matrix and grains of this lithofacies, and dark-colored organic flakes fill the matrix (Fig. 2a–e). Trace fossils of benthic fauna were not found in the organic-rich black shale intervals of the lower members of the Longmaxi and Wufeng formations, thus implying a deepwater anoxic environment. Siliceous skeletal fragments consisting of radiolarian and sponge spicules that live in the oxygenated interval of the water column can also be found in the rocks (Fig. 2a). These fragments could have been transported into the deeper part of the sedimentary basin together with the detrital quartz and feldspar. Authigenic minerals, including quartz, calcite, dolomite, and pyrite framboids are also present and characterized by euhedral crystal morphology (Fig. 2 b and d).

The TOC content of core shale samples ranges from 0.5% to 5.9% (Table 1). The results of the maceral analysis indicate that the predominant maceral of organic fraction is micrinite (e.g., crumb and flocculent cluster), which is interpreted as the residues after oil generation and expulsion [11], and pyrobitumen formed by the cracking of retained oil [40]. The *VRr* ranges from 2.8% to 3.0% (Table 1) within the dry gas generation window.

The data for the core shale samples listed in Table 1 indicate that their mineral compositions are different. Sample Nos. 1 to 2 and 7 to 8 are relatively richer in carbonate than Nos. 3 to 6 (Fig. 3). In particular, the carbonate content of Sample No. 8 is 69%, thus indicating an argillaceous carbonate rock lithofacies. The brittle mineral (quartz + feldspar + carbonate) levels of all samples range from 56% to 84%, suggesting good stimulation capacity. The clay composition of all samples is slightly low between 14% and 40%, and no apparent correlation is found between the TOC and total clay content. The quartz content of shale samples (Nos. 1–7) varies from 18% to 40% and shows a positive relationship with TOC (Fig. 4a). Combined with the appearance of siliceous skeletal fragments, the positive relationship between TOC and quartz indicate that some of them have biogenic origins [41]. Furthermore, the pyrite content shows a strong positive relationship with TOC, particularly when the TOC content is less than 3% (Fig. 4b); on the other hand, the TOC is generally increasing with depth, thus indicating the oxygen level of basal Wufeng–Longmaxi formation is much lower than that of the upper parts.

### 4.2. Pore types and total porosity

Three pore types can generally be found in gas shale reservoirs, namely, intraparticle organic pores, intraparticle, and interparticle pores [1,42]. Furthermore, cracks that can be caused by shrinkage in clay minerals and/or decompression effects after the retrieval from subsurface are frequently observed [5]. The classification of pore types in this study was based on [1,42]. The cracks between clay minerals were classified as interparticle pores for simplicity. Fig. 5a and b demonstrate the interparticle pores of gas shale reservoir preserved in clay mineral floccules [43] and shrinking of clay minerals [5]. The pores preserved in the floccules of clay minerals are characterized by an irregular distribution and angular shapes. The pores caused by the perfect cleavage (001) of clay minerals are mainly slab-shaped and have good connectivity.

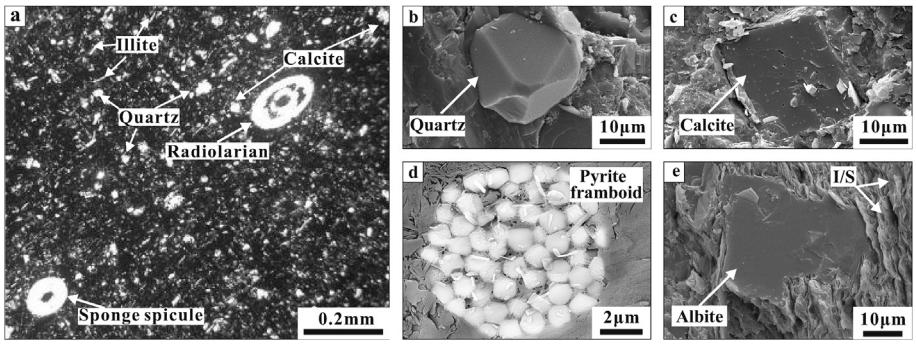


**Fig. 2.** Mineral compositions of the Wufeng–Longmaxi gas shale reservoir. a) Texture of organic-rich shale, fine quartz silts, siliceous skeleton fragments, carbonate minerals, and clay minerals from the matrix. The dark-colored flakes are organic matters. b) and c) Quartz and calcite of euhedral crystal morphology. d) Pyrite framboid. e) Partly argillized albite particle and mixed-layer minerals of illite and smectite (I/S), thus indicating that some feldspar have transformed into clay minerals during diagenetic processes. b), c) and e) are second electron images, d) is back scattered electron image.

Interparticle pores that develop at the margin of large particles are rare. These pores associated with mineral grain boundaries tend to be relatively large in long axis, thus making them similar to cracks in shape (Fig. 5c and d). Although these pores are uncommon overall, their clusters can be observed locally in some silt-bearing laminae.

Fig. 5e and f demonstrate the intraparticle pores that develop within mineral grains. Their shapes usually vary from nearly spherical to irregularly polygonal and are distributed within the grains randomly. The intraparticle pores are probably caused by dissolution or crystallographic defects based on their morphology and developed location.

Intraparticle organic pores are important for gas shale reservoirs; this pore type constitutes the most widespread and numerous pore types in the mature Barnett Shale [1]. These pores are also frequently present in Wufeng–Longmaxi black shales (Fig. 6). Given that pores are associated with organic matter, their characteristics are closely related to the occurrence and distribution of organic matter. Two types of organic matter occurrence are observed in studied samples, namely, separate particles distributed in the shale matrix and aggregates located within the pyrite framboids (Fig. 6). Therefore, the intraparticle organic pores can be observed within both separate organic matter particles and pyrite framboids. Pore size and shape vary widely. The size distribution observed in the studied samples varies from very fine mesopores to macropores, and shapes vary widely (Fig. 6b and d).

Although FE-SEM imaging can provide a large amount of qualitative information on the reservoir parameters of black shales, including pore types, shapes, coordinate numbers, and surface porosity, the total porosity is usually determined by the difference between the bulk and grain densities [5,35] for the strong bulk heterogeneity of shales. The total porosity of the eight samples ranges from 1.8% to 5.3% (Table 2). These values are comparable with the porosity range of North American gas shale reservoirs [5]. Except for Sample No. 8, the total porosity of the other samples shows a good positive correlation with TOC and a weaker positive correlation with total clay minerals content (Fig. 7a and b); thus, organic matter pores significantly contributes to the total porosity. Sample No. 8 has the highest TOC (5.9%) (Table 1) but its total porosity is low (Table 2), thus indicating that the TOC is not the main controlling factor for its porosity. Our limited dataset cannot provide definite reasons on this discrepancy; thus, detailed studies on the relationships between TOC and porosity in this type of argillaceous carbonate rock should be conducted in the future.

### 4.3. Pore structure

The low-pressure nitrogen adsorption and conventional MIP are two widely used methods for pore characterization. The low-pressure nitrogen adsorption can characterize the pore size ranges from 1.7 nm to 193.5 nm; thus, the total pore volume indicated is the pore volume less than 193.5 nm [8], whereas the MIP can record the information of pore size ranges from 3.5 nm to 500 μm [7]. Nevertheless, the two methods are different because low-pressure nitrogen adsorption provides a pore-body distribution [44], whereas MIP is essentially a pore-throat measurement [8].

Gas shale reservoirs as typical heterogeneous porous media have wide PSD; thus, the conjunction of gas adsorption and MIP methods can obtain the most comprehensive description of pore structures [8].

#### 4.3.1. Mercury injection capillary pressure curve and pore-throat size distribution

Despite current instruments that can reach 400 MPa at the smallest pore-throat size of 3.6 nm, the mercury compresses the rock structure and significantly affects the data at this high pressure condition [8]. Therefore, the MIP pressures in this study do not exceed 50 MPa and the smallest diameters of pore-throats are not smaller than 20 nm. The capillary pressure curves of the eight samples all have similar shapes (Fig. 8). The intrusion curves of all samples increase sharply when the capillary pressure ($Pc$) interval ranges from $0.01 \times 10^5$ Pa to $1 \times 10^5$ Pa, whereas the mercury intrusion volume fraction ($S_{Hg}$) increases with increasing $Pc$. The curves are K-shaped, thus indicating that the pore-throat sizes are unhomogeneous. Similar to the intrusion curves, the extrusion curves are K-shaped. Furthermore, both the intrusion and extrusion capillary pressure curves have flatter slopes when the $Pc$ is larger than $1 \times 10^5$ Pa than when $Pc$ is between $0.01 \times 10^5$ and $1 \times 10^5$ Pa. Thus, most of the sample pore volume is made up of pores with throats less than 50 nm. Nevertheless, compared with the total pore volume of studied samples, pores with throats larger than 20 nm contribute less to pore volume ($<4 \times 10^{-4}$ $cm^3/g$) (Fig. 8), thus implying that the main pore volume should be contributed by pores with throats smaller than 20 nm.

#### 4.3.2. Low-pressure nitrogen adsorption

The low-pressure nitrogen adsorption method was used to measure the organic-rich shale samples and obtain the distribution and volumes of pores smaller than 20 nm. Nitrogen

**Table 1**
TOC, equivalent *VRr*, and mineralogical composition.

| Samples | Depth (m) | TOC (%) | VRr (%) | Relative percentage (%) | | | | | | | | |
|---|---|---|---|---|---|---|---|---|---|---|---|---|
| | | | | Quartz | Feldspar | Carbonate | Pyrite | Clays[a] | Illite | Kaolinite | Chlorite | I/S[b] |
| No.1 | 2382 | 0.5 | nd.[c] | 18.0 | 3.8 | 46.7 | 0.6 | 30.9 | 22.2 | 0.6 | 4.9 | 3.2 |
| No.2 | 2394 | 0.8 | nd. | 23.6 | 5.6 | 34.2 | 1.1 | 35.5 | 21.4 | 0.8 | 6.5 | 6.8 |
| No.3 | 2467 | 1.2 | nd. | 35.2 | 14.8 | 11.6 | 1.3 | 37.1 | 25.9 | 0.8 | 5.6 | 4.8 |
| No.4 | 2474 | 0.9 | 2.8 | 30.4 | 19.7 | 14.4 | 1.4 | 34.1 | 22.8 | 0.7 | 1.7 | 8.9 |
| No.5 | 2487 | 2.0 | 2.8 | 37.1 | 6.0 | 14.4 | 2.2 | 40.3 | 27.4 | 0.8 | 1.2 | 10.9 |
| No.6 | 2496 | 4.1 | 2.8 | 40.0 | 6.1 | 11.3 | 2.5 | 40.1 | 27.6 | 1.1 | 3.5 | 7.9 |
| No.7 | 2499 | 3.9 | 3.0 | 30.9 | 4.0 | 20.9 | 6.4 | 37.8 | 27.1 | 0.6 | 2.4 | 7.7 |
| No.8 | 2511 | 5.9 | 3.0 | 13.2 | 2.0 | 69.2 | 1.3 | 14.3 | 10.2 | 0.3 | 0.4 | 3.4 |

[a] Total clays = Illite + Kaolinite + Chlorite + I/S.
[b] Mixed-layer minerals of illite and smectite.
[c] No data.

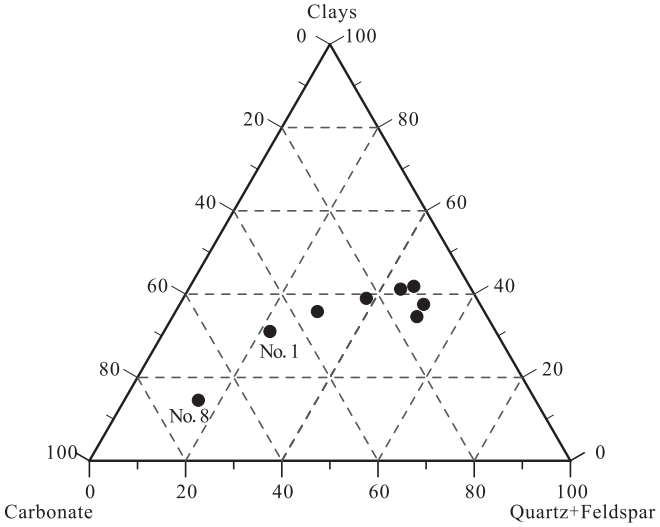


**Fig. 3.** Ternary diagram that shows the mineralogical composition of the black shale core samples.

adsorption and desorption were investigated at a temperature of −195.85 °C and *P*/*Po* of approximately one. The isotherms are shown in Fig. 9. The adsorption amount varies from 7.82 $cm^3/g$ to 17.68 $cm^3/g$ for different samples and shows a positive relationship with TOC (Fig. 10). Isotherms for all samples show a hysteresis pattern and a plateau at high *P*/*Po* similar to the Type IV isotherm, which is associated with the capillary condensation in mesopores and indicates that mesopores are an important contribution to pore volume [37].

The hysteresis loops for the eight samples show that they are Type H2, which used to be attributed to the mechanism difference between the condensation and evaporation processes in pores with narrow necks and wide bodies (often referred to as “ink bottle” pores) but is now associated with pore network effects [37]. Therefore, the isotherm shapes and hysteresis loops of samples demonstrate that the Wufeng–Longmaxi gas shale reservoir has a complex pore system and strong heterogeneity.

### 4.3.3. Specific surface area and pore volume

Except for sample No. 8, the total specific surface area ($S_{BET}$) of the other samples ranges from 9.6 $m^2/g$ to 18.9 $m^2/g$ (Table 2). $S_{BET}$ shows a good positive relationship with TOC (Fig. 10). This relationship type has been observed for many North American gas shale reservoirs [11,35] and the Lower Silurian Longmaxi shale in China (Tian, 2013). The pore volume and $S_{BET}$ of the seven black shale samples range from 0.011 $cm^3/g$ to 0.020 $cm^3/g$ (Table 2) and also shows a good positive relationship with TOC. Otherwise, a weak positive relationship existed among the total specific area, pore volume, and total clay mineral content, thus indicating that clay minerals somehow contributes to the total specific area and pore volume.

### 4.3.4. Pore size distribution (PSD)

The pore size of the core shale samples was calculated by using the Barret–Joyner–Halenda (BJH) model based on the desorption branch of the isotherms. The average pore size ranges from 2.9 nm to 3.9 nm (Table 2), and a plot of the pore diameter (*dV*/*dW* versus *W*) with respect to the derivative of pore volume is shown in Fig. 11. This plot shows that the peak pores of all

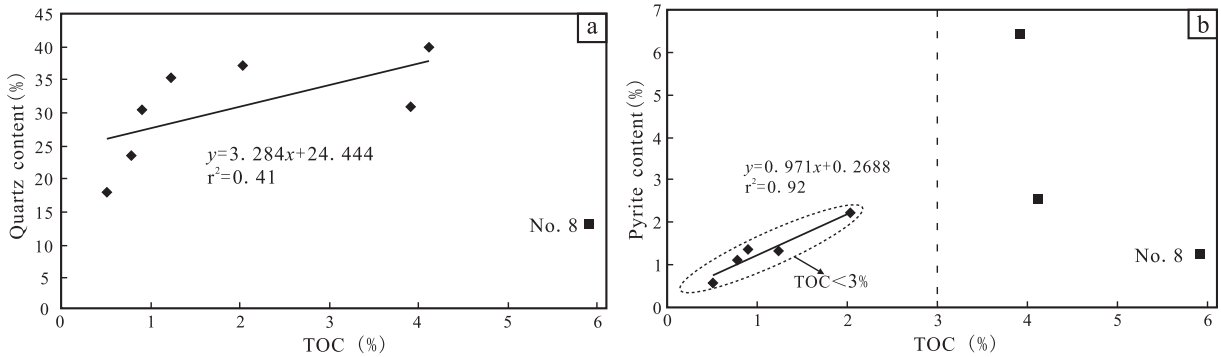


**Fig. 4.** Interrelationships between TOC and quartz content and between TOC and pyrite content. a) TOC vs. quartz diagram. The quartz content shows a weak positive correlation with TOC, but Sample No. 8 (organic-rich argillaceous carbonate rock) does not follow this trend. b) TOC vs. pyrite diagram. When the TOC content is less than 3%, the pyrite content shows a strong positive correlation with TOC, but the samples with TOC content higher than 3% do not follow this trend.

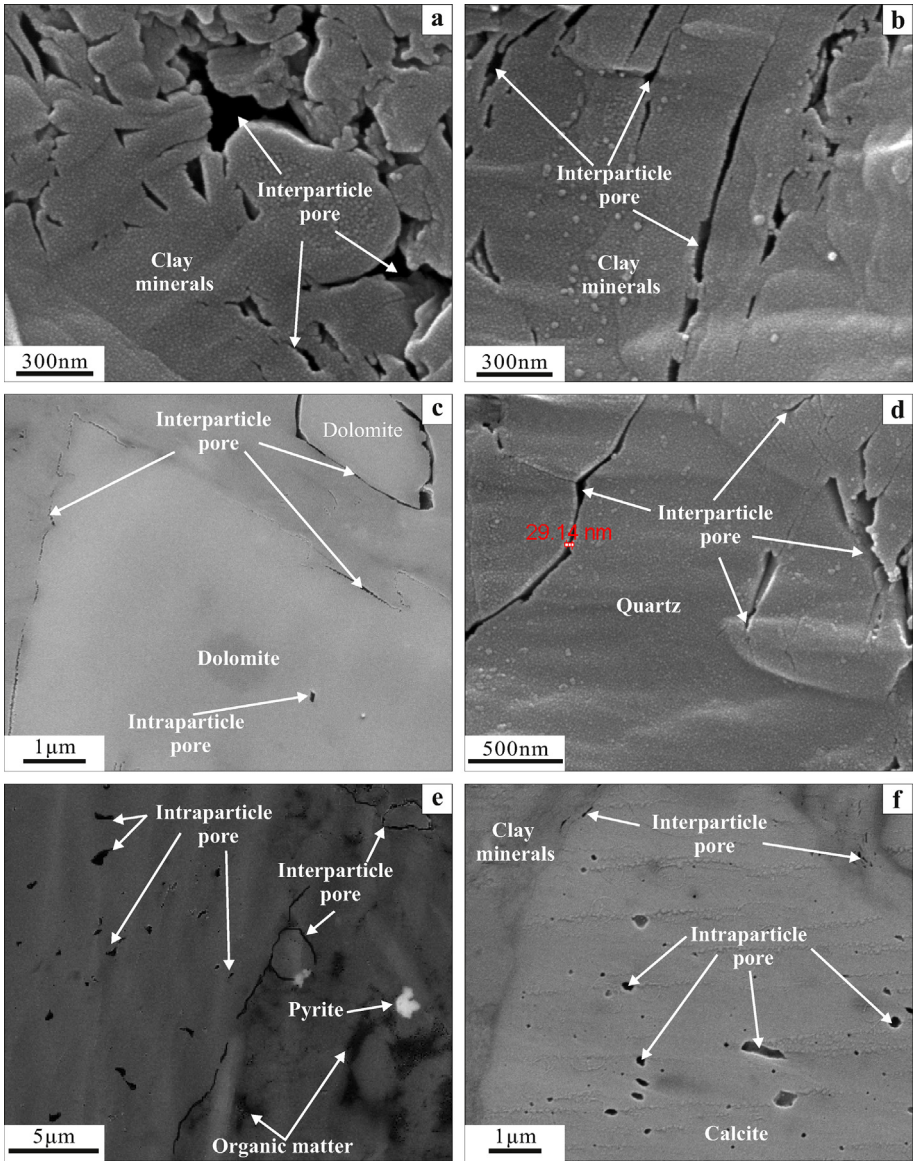


**Fig. 5.** FE-SEM images of different pore types. a) The angular pores between clay mineral crystals. b) Pores (cracks) caused by the shrinking of clay minerals during diagenesis present in the slab-shape. c) Interparticle pores develop at the margins of euhedral dolomite crystals, and some intraparticle pore can also be found. d) Interparticle pores at the margins of quartz silt grains. e) Intraparticle pores within feldspar grain. The light spot is pyrite, whereas the dark grains are organic matter. f) Intraparticle pores within calcite grain. Several interparticle pores between clay minerals are also shown. a), b), and d) are secondary electron images, whereas c), e), and f) are back scattered electron images.

samples are less than 4 nm in diameter and the concentration decreases with increasing pore size, thus indicating that pores in the size range of 3 nm–4 nm mainly contribute to the pore volume. These observations are consistent with the results of many gas shale reservoirs in North America [5] and the Lower Silurian Longmaxi gas shale reservoirs in China (Tian, 2013).

## 5. Discussion

### 5.1. Origins and significance of nanopores

The MIP and low-pressure nitrogen adsorption data sets indicate that the nanopores primarily contribute to the pore volume of the Wufeng–Longmaxi gas shale reservoir. We observed three types of nanopores as intraparticle organic pore, interparticle pore, and intraparticle pore in the studied samples according to the pore type classification suggested by Refs. [1,42].

Since the intraparticle organic nanopores first identified in the mature Barnett shale, they have been believed to be the main contributors to the pore volume in a mature gas shale reservoir [1]. Similar organic nanopores that occur in many other gas shale reservoirs have also been documented, such as the Woodford, Haynesville, and Marcellus [5,15]. The clear positive correlation between TOC and pore volume in the present study implies that intraparticle organic nanopores are the main contributors to pore volume in the Wufeng–Longmaxi gas shale reservoir. The abundance of nanopores developed in grains of organic matter usually has a strong correlation with vitrinite reflectance, thus suggesting that pore formation originates from the thermal maturation and conversion of organic matter (e.g., kerogen) [1]. During the catagenesis ($0.5 < Ro < 2.0$) stage [45], the thermal

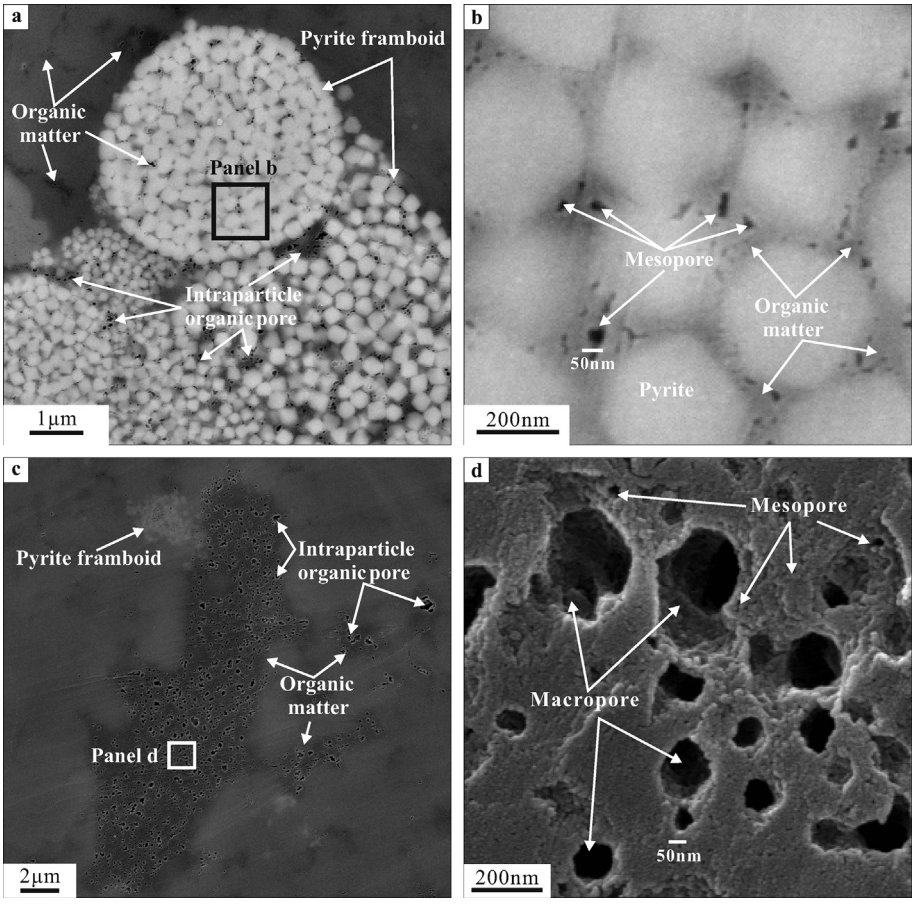


**Fig. 6.** Morphology of intraparticle organic pores. a) Two types of organic matter particles are observed, including separate particles distributed in the shale matrix and organic matter aggregates located within the pyrite framboids. Intraparticle organic pores developed well within both types of organic matter particles. b) Intraparticle organic mesopores developed within pyrite framboids. c) Separate organic particles within the shale matrix have well-developed intraparticle organic pore systems. d) The pores within organic particles have a wide-size distribution interval, ranging from fine mesopores (<10 nm) to macropores. All photos were taken in second electron model.

maturation and conversion of organic matter lead to the breaking of chemical bonds of the aliphatic component of kerogen and the simultaneous formation of hydrocarbons and intraparticle organic nanopores [40]. Given that the convertible organic carbon of TOC largely depends on the organic-matter type, the variability in the organic matter source can largely influence the amount of porosity development [1]. The alginites in kerogen usually have more hydrogen than other macerals; thus, the alginite rich kerogen (conversion rate of organic matter at over 50%) has a large capacity to generate hydrocarbons [45] and simultaneously form a large pore volume [1]. Although the strong-degradation of organic matter destroys the maceral structure of kerogen of the Wufeng–Longmaxi shale, the previous studies suggested that the kerogen of Wufeng–Longmaxi shale belong to Type $II_1$ [19]. The thermal maturity of organic matter in all samples are within a dry gas window (VRr = 2.79%–3.02%), thus implying that the Wufeng–Longmaxi shale have undergone deep burial diagenesis and strong thermal decomposition. The result is that a large quantity of organic matter has been converted into hydrocarbons and may create many secondary pores because of the conversion of organic matter dispersed in the rock (Fig. 6). The PSD of intraparticle organic pores varies widely, and many mesopores and macropores are observed to be closely associated with each other (Fig. 6c and d). This phenomenon has been observed frequently in North American gas shale reservoirs [1,5]. Similar

**Table 2**
Physical properties of the Wufeng–Longmaxi gas shale reservoir.

| Samples | Depth (m) | $P$ (%) | $S_{BET}$ ($m^2$/g) | $d_{BJH}$ (nm) | $V$ ($cm^3$/g) | Gas content ($m^3$/ton) | Adsorbed gas (%) | Gas-filled porosity (%) |
|---|---|---|---|---|---|---|---|---|
| No. 1 | 2381.6 | 1.8 | 11.2 | 3.7 | 0.013 | 1.5 | 54 | 1.2 |
| No. 2 | 2394.2 | 2.3 | 12.6 | 3.9 | 0.014 | 1.4 | 59 | 1.1 |
| No. 3 | 2467.3 | 1.9 | 12.0 | 2.9 | 0.012 | 2.7 | 44 | 1.7 |
| No. 4 | 2473.9 | 2.2 | 9.6 | 3.7 | 0.011 | 2.4 | 45 | 2.0 |
| No. 5 | 2486.8 | 4.6 | 16.0 | 3.1 | 0.017 | 3.3 | 64 | 4.1 |
| No. 6 | 2496.4 | 5.3 | 18. 9 | 3.9 | 0.020 | 3.4 | 82 | 4.6 |
| No. 7 | 2499.1 | 5.1 | 18.8 | 3.7 | 0.020 | 3.1 | 76 | 4.2 |
| No. 8 | 2511.4 | 4.2 | 14.7 | 3.5 | 0.016 | 3.1 | 78 | 4.2 |

$P$ – total porosity; $d_{BJH}$ – average diameter determined using the BJH method; $V_{BJH}$ – pore volume. The data of gas content and adsorbed gas was tested by Research Institute of Petroleum Exploration and Development, CNPC.

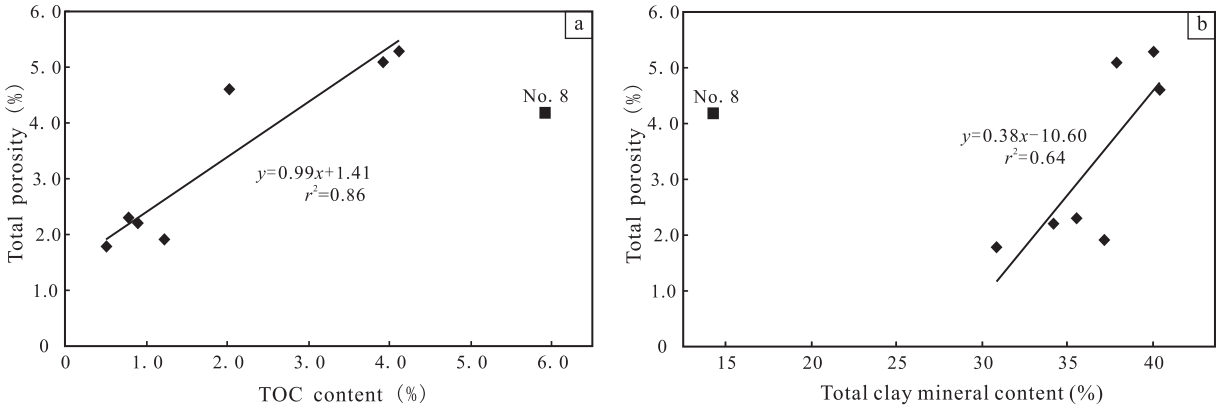


**Fig. 7.** Relationship between TOC and total porosity and total clay mineral and total porosity. a) Positive relationship between total porosity and TOC. b) The positive relationship between total porosity and clay mineral is weaker than that between TOC and total porosity.

reports about the Longmaxi shale have been published recently [13,43].

In addition to intraparticle organic pores, matrix interparticle and intraparticle pores are also shown in the FE-SEM images. The slit-shaped interparticle pores are associated with the interlayered space caused by a perfect cleavage (001) of clay minerals (Fig. 5a and b) and along grain boundaries between clay and brittle mineral grains (Fig. 5c and d). The pores preserved in clay mineral floccules are another type of interparticle pores that are widely developed in Barnett and Woodford shales [43]. Similar pores that are characterized by irregular distribution and angular shapes can also be found in the Wufeng–Longmaxi shale (Fig. 5a). Intraparticle pores are usually developed within feldspar and carbonate mineral grains (Fig. 5e and f), which are probably caused by dissolution or crystallographic defects. Dissolution-originated intraparticle pores have been frequently observed in gas shale reservoirs in North America [1,5,42,43].

Most of the long axes of slit-shaped nanopores are parallel to the laminae, particularly the pores associated with the interlayer space of clay minerals. The alignment of platy mineral grains can be the predominant control factor on the anisotropy of gas shale reservoirs. This conclusion is supported by the permeability anisotropy of gas shale reservoirs, wherein a high permeability is measured parallel to the laminae and a low permeability is measured orthogonal to laminations [46].

### 5.2. Impact of nanopores on shale gas enrichment

Shale gas may be stored in organic rich shales in three forms: as free gas in natural fractures and intergranular porosity, as gas sorbed onto kerogen and clay-particle surfaces, or as gas dissolved in kerogen and bitumen [48]. Nanopores are the main contributor of gas storage space of Wufeng–Longmaxi shale reservoir, their characteristics strongly impact the enrichment form of shale gas. Previous studies interpreted that specific surface areas and pore volumes are mainly controlled by pore structure, in coarse mesopres and macropores the natural gas molecules usually stored in non-sorbed state, whereas in smaller pores (e.g. fine mesopores and micropores) the natural gas molecules will be captured and stay in sorbed state on the surface of adsorbate due to enhanced adsorbent–adsorbate interaction [1,8,11,13,21,37]. As we discussed before, the deep burial diagenesis lead to the organic matter of Wufeng–Longmaxi shale has evolved in over matured state, and formed large quantity of fine mesopores (smaller than 4 nm). They act as the predominant contributor of pore volume and specific surface area in Wufeng–Longmaxi gas shale reservoirs in study area (Table 2, Fig. 11), leading to a high adsorption capacity of organic rich shales. Gas contents of studied samples range from 1.4 to 3.4 $m^3$/ton, while the adsorbed gas takes high proportions (44%–82%, mean = 63%) (Table 2), indicating the adsorbed gas is a main stored form in this reservoir. The adsorbed gas contents of studied samples are comparative to that of many gas shale reservoirs in the United States, and higher than that of the Wufeng–Longmaxi gas shale reservoirs in the Eastern Sichuan Basin (Table 3).

The fine nanopores related to thermal maturity of organic matter in studied samples provide enough space for natural gas accumulation. When compared with the gas shale reservoirs that have been commercially developed, we find that the properties of the studied reservoir have reached the threshold for commercial shale gas production (Table 3). The studied samples of TOC >2% may have good capacity for production, for their natural gas contents are over 3 $m^3$/ton (Table 2). Actually, this inference has been proved by production testing implemented very recently. Fig. 12 shows the gas production curves of the production testing, the gas productions of vertical well and horizontal well fluctuate around $1.5 \times 10^4$ $m^3$/day/well (with maximum ~$3.5 \times 10^4$ $m^3$/day/well) and $12.5 \times 10^4$ $m^3$/day/well (with maximum ~$40 \times 10^4$ $m^3$/day/well), respectively. These values are comparative to that of the Jiaoshiba shale gas field (production testing of horizontal well = $11–50 \times 10^4$ $m^3$/day/well; production>$6 \times 10^4$ $m^3$/day/well), the first shale gas productivity construction area in China [31]. The data sets of reservoir characteristics from studied appraisal well indicate a good natural gas potential, hence this well can be used as a reference for future exploration and production in this area.

### 5.3. Potential risks for shale gas exploration in the Southern Sichuan Basin

The hybrid techniques applied to characterize the pore structure of Wufeng–Longmaxi gas shale reservoirs in the Southern Sichuan Basin can help us to better understand the gas potential, transportation, and accumulation mechanisms. Moreover, the data sets from the studied well show that the characteristics of organic-rich gas shale intervals are comparable with the commercially developed shale gas plays in North America, thus indicating that the Wufeng–Longmaxi formation has good natural gas potential. Nevertheless, some risks should be considered, such as the petrological properties of shales, thermal maturation of organic matter, and tectonic movements.

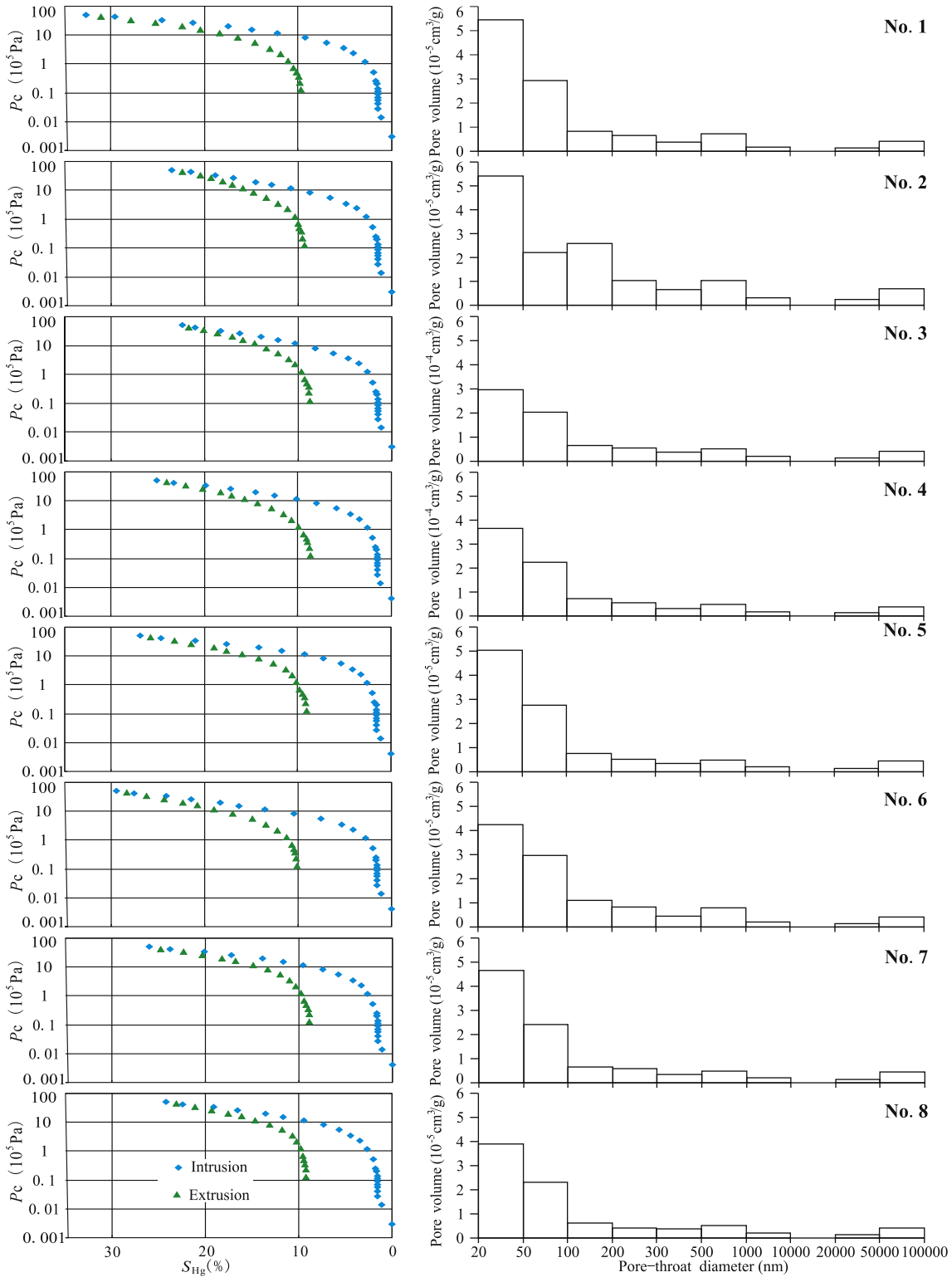


**Fig. 8.** Mercury injection capillary pressure curves and pore-throat distribution.

The petrological properties of gas shale reservoirs are mainly derived from brittle mineral content (i.e., the most important factor that determines the reservoir stimulation) and organic carbon content (i.e., the most important factor that determines gas sorption capacity and content) [1,2,5,20,47]. The brittleness of gas shale reservoirs are mainly related to carbonates and quartz, and the reduction in quartz and carbonate contents and/or change in quartz origin (detrital vs. biogenic) can be an important risk for shale gas exploration and production [21]; and references therein). The high content of carbonate minerals possibly does not indicate a good gas resource potential because most carbonates are produced within the photic zone (~100 m),

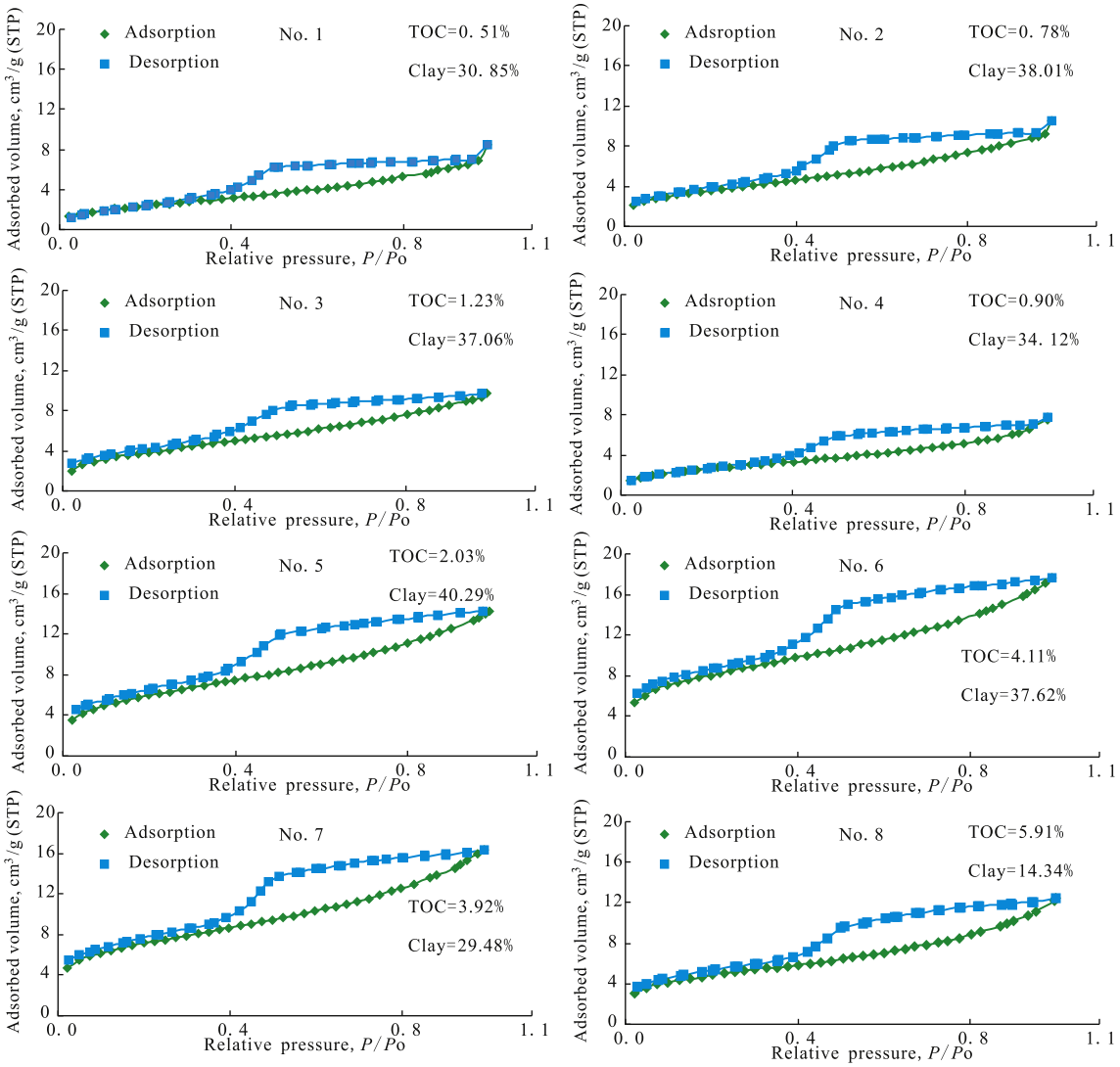


**Fig. 9.** Low pressure nitrogen adsorption and desorption isotherms (T = −195.85 °C).

where primary productivity is higher and richer in oxygen [48]. This condition is unfavorable for organic matter preservation. The wide variation in TOC contents in shales (Table 3) are mainly caused by changes in redox condition and/or primary productivity of sea water, whereas the reduction in TOC contents is a major risk for gas resource potential. Therefore, identifying the intervals of proper brittle mineral and TOC content is important in shale gas exploration and production.

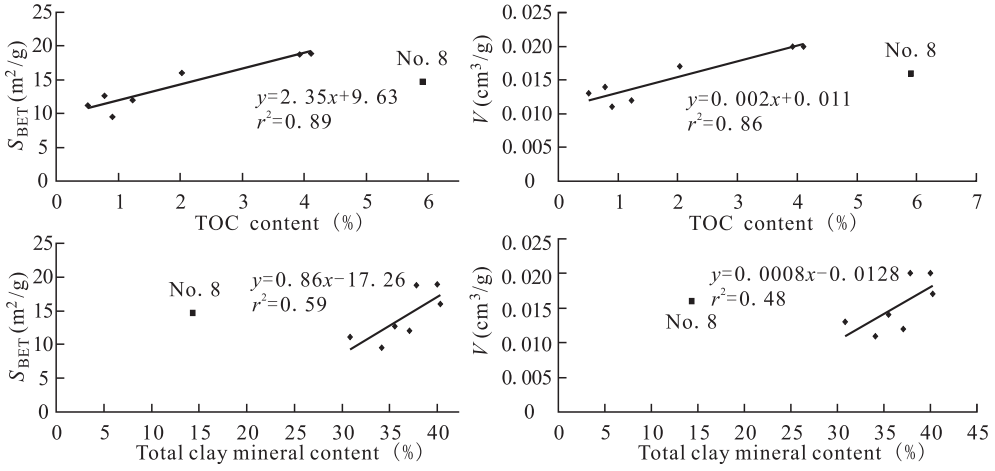


**Fig. 10.** Relationships of TOC and total clay mineral content with $S_{BET}$ and $V_{BET}$.

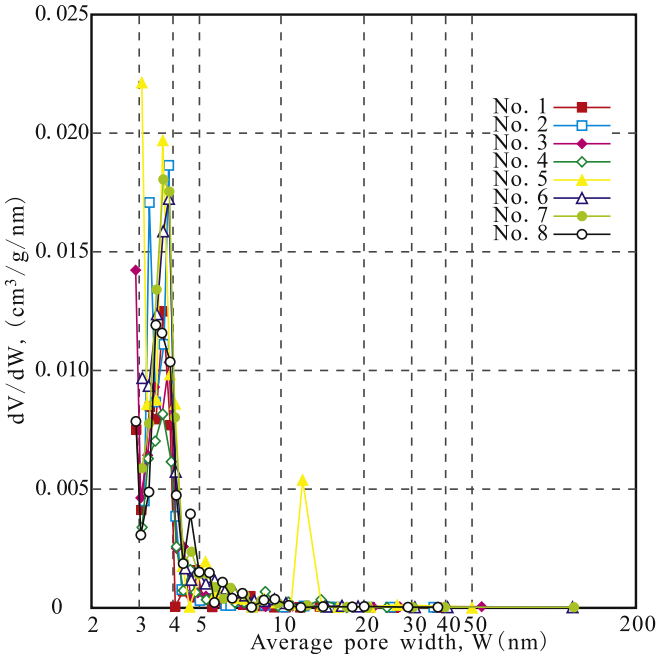


**Fig. 11.** Pore volume distribution with BJH pore sizes.

Generation of hydrocarbons and intraparticle organic nanopores are originated with the maturation of organic matter [1,40], so the organic-rich shale of higher maturity is appropriate for gas potential. The maturities of organic matter in many commercial shale gas plays are within the dry gas window (Table 3). Similarly, the maturities of organic matter in the Wufeng–Longmaxi shale are more than 2%, thus indicating that a significant amount of natural gas has been generated at the peak of gas generation. Large quantities of intraparticle organic nanopores are also simultaneously formed. Nevertheless, the higher the organic matter maturity, the natural gas potential is not necessarily the better. Given that organic matter maturity is typically related to the burial depth of organic shales, the higher the maturity of organic matter, the deeper the strata are buried. The compaction of thick overlying strata may shut down some intraparticle organic nanopores, which decreases the storage capacity of natural gas. This phenomenon was observed in the core shale of Early Cambrian black shale (Ro > 4.0%, unpublished data). Therefore, organic-rich shales with extremely high maturity may be a potential risk for exploration.

The Upper Ordovician-Lower Silurian (Wufeng–Longmaxi formation) organic-rich shales in southern China have experienced several major orogenic events (e.g., Caledonian, Variscan, Indo-Sinian, Yanshanian, and Himalayan movements) after the sedimentation of the Longmaxi formation [49]. These tectonic movements caused a strong deformation of strata and fluctuation of burial depth; in particular, orogeny occurred at approximately 130 Ma (Late Yanshanian) and 23 Ma (Himalayan) [49]. They were characterized by intense uplift, erosion of overburden rocks, and faulting, which lead to the loss of free gas [21]. If the retained free gases stored in mesopores, macropores, and fractures were lost during uplift/erosion and rock relaxation, the total gas content would be lower than the present-day gas sorption capacity of the shale [21]. This implication has been supported by the exploration results in southern China. Therefore, the loss of free gas because of epigenetic erosion, fracturing, and faulting is a major risk for shale gas exploration.

In summary, the shale gas exploration in the southern Sichuan Basin is still at its initial stage. The pore system characteristics and reservoir indices of the Wufeng–Longmaxi organic-rich shale are comparable with commercial shale gas plays. The production testing of the studied appraisal effectively demonstrates good resource potential, but risks still exist. Therefore, more extensive studies on over-mature gas shale reservoirs should be promoted to benefit future shale gas exploration and production.

## 6. Conclusions

The petrology and pore system characteristics of core shale samples collected from the Upper Ordovician-Lower Silurian Wufeng–Longmaxi formation in the south margin of the Sichuan Basin were studied using microphotometric, FE-SEM observation, mercury porosimetry, and low-pressure nitrogen adsorption methods. The following conclusions have been drawn:

(1) The brittle mineral compositions of the Wufeng–Longmaxi gas shale reservoir are higher than 55%, thus indicating good stimulation capacity. The positive relationships between TOC and quartz, together with the existence of fossils organisms, indicate that they have partially biogenous origin at the very least.
(2) The intraparticle organic nanopores that originated in the decomposition of organic matter mainly contribute to the pore volume and specific surface area. In particular, the intervals with TOC content higher than 2% have good gas potential and their gas content is more than 3 $m^3$/ton.

**Table 3**
General properties of gas shale reservoirs in the United States and China.

| Shale gas play | Depth (m) | Net thickness (m) | TOC (%) | Ro (%) | Total porosity (%) | Gas-filled porosity (%) | Adsorbed gas (%) | Gas content ($m^3$/ton) | Production ($10^4$ $m^3$/day/well) |
|---|---|---|---|---|---|---|---|---|---|
| Antrim | 183–732 | 21–37 | 0.3–24 | 0.4–0.6 | 9.0 | 4 | 70 | 1.1–2.8 | 0.11–1.42 |
| Ohio | 610–1524 | 9–30 | 0–4.7 | 0.4–1.3 | 4.7 | 2 | 50 | 1.7–2.8 | 0.17–0.28 |
| New Albany | 183–1494 | 15–30 | 1–25 | 0.4–1.0 | 10–14 | 5 | 40–60 | 1.1–2.3 | 0.11–0.23 |
| Barnett | 1981–2591 | 15–61 | 4.5 | 0.5–2.0 | 4–5 | 2.5 | 35–50 | 8.5–9.9 | 0.85–0.99 |
| Lewis | 914–1829 | 61–91 | 0.45–2.5 | 1.6–1.88 | 3–5.3 | 1–3.5 | 60–85 | 0.4–1.3 | 0.04–0.13 |
| Marcellus | 1219–2591 | 15–61 | 3–12 | 0.4–1.3 | 10.0 | Nd. | Nd. | 1.7–2.8 | 8.78 |
| Woodford | 1829–3353 | 37–67 | 1–14 | 1.1–3.0 | 3–9 | Nd. | Nd. | 5.7–8.5 | 1.18 |
| Sichuan (E) | 2313–2595 | 38–42 | 2.5–3.5 | 2.2–3.0 | 1.2–7.2 | Nd. | 35–47 | 0.44–5.19 | >6.00 |
| Sichuan (S) | 2390–2516 | 32 | 0.5–5.9 | 2.79–3.02 | 3.58–4.85 | 1.1–4.6 | 44–82 | 1.35–3.42 | nd. |

Data of Antrim, Ohio, New Albany, Barnett, and Lewis are from Ref. [47]. Data of Marcellus and Woodford are from Ref. [52]. The adsorbed gas data of Barnett are from Ref. [2]. The data of Sichuan (E) are from the Jiaoshiba shale gas field (Wufeng–Longmaxi formation), which is the first shale gas productivity construction area in China [31]. The data of Sichuan (S) are from the well used in this study. "Nd." means that the data are absent in the cited reference, (E) means the Eastern Sichuan Basin, and (S) means the Southern Sichuan Basin.

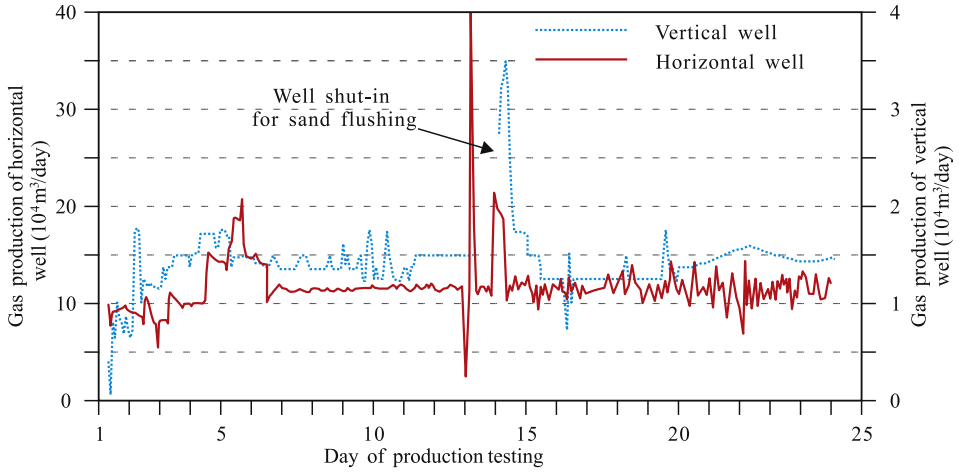


**Fig. 12.** Gas yield curves of the production test of vertical and horizontal wells.

Moreover, production testing shows that the gas production of the appraisal well is comparable with the commercial gas shale plays in North America.

(3) Pores size of Wufeng–Longmaxi shale ranges from several nanometers to micrometers, although the predominant pores have sizes smaller than 4 nm. The studied samples have total surface areas ($S_{BET}$) that range from 9.6 m$^2$/g to 18.9 m$^2$/g, thus indicating good gas sorption capacity (i.e., adsorbed gas ranges from 44% to 82%).

(4) The shale gas resource potential in this area is significant. Nevertheless, exploration of study area faces many uncertainties because of poor understanding on shale gas accumulation controls. Extensive studies on over-mature gas shale reservoirs should be conducted in the future to avoid exploration and production risks.

## Acknowledgments

The authors are grateful to Lei Xie, Xiaowei Yang, Bing Shu and Yanni Ma, for their help in sampling and field work. This study was supported by the National Natural Science Foundation of China (Grant No. 41302123), the Doctoral Program of Higher Education (Specialized Research Fund) of China (Grant No. 20125121130001), and the Science Foundation of Education Department of Sichuan Province (Grant No. 13ZB0190).

## References

[1] R.G. Loucks, R.M. Reed, S.C. Ruppel, D.M. Jarvie, Morphology, genesis, and distribution of nanometer-scale pores in siliceous mudstones of the mississippian barnett shale, J. Sediment. Res. 79 (2009) 848–861, http://dx.doi.org/10.2110/jsr.2009.092.

[2] S.L. Montgomery, D.M. Jarvie, K.A. Bowker, R.M. Pollastro, Mississippian barnett shale, fort worth basin, north-central Texas: gas-shale play with multi–trillion cubic foot potential, AAPG Bull. 89 (2) (2005) 155–175, http://dx.doi.org/10.1306/09170404042.

[3] C.R. Clarkson, M. Freeman, L. He, M. Agamalian, Y.B. Melnichenko, M. Mastalerz, R.M. Bustin, A.P. Radlinski, T.P. Blach, Characterization of tight gas reservoir pore structure using SANS/SANS and gas adsorption analysis, Fuel 95 (2012) 371–385, http://dx.doi.org/10.1016/j.fuel.2011.12.010.

[4] C.R. Clarkson, N. Solano, R.M. Bustin, A.M.M. Bustin, G.R.L. Chalmers, L. Hec, Y.B. Melnichenko, A.P. Radlinski, T.P. Blach, Pore structure characterization of North American shale gas reservoirs using USANS/SANS, gas adsorption, and mercury intrusion, Fuel 103 (2013) 606–616. http://dx.doi.org/10.1016/j.fuel.2012.06.119.

[5] G.R.L. Chalmers, R.M. Bustin, I.M. Power, Characterization of gas shale pore systems by porosimetry, pycnometry, surface area, and field emission scanning electron microscopy/transmission electron microscopy image analyses: examples from the Barnett, Woodford, Haynesville, Marcellus, and doig units, AAPG Bull. 96 (6) (2012a) 1099–1119, http://dx.doi.org/10.1306/10171111052.

[6] L. Robert, J.R. Burwell, Physical chemistry division commission on colloid and surface chemistry definitions, terminology and symbols in colloid and surface chemistry partII: heterogeneous catalysis (rules approved 1975), Pure Appl. Chem. 46 (1976) 71–90.

[7] H. Giesche, Mercury porosimetry: a general (practical) overview, Part. Part. Syst. Charact. 23 (1) (2006) 9–19, http://dx.doi.org/10.1002/ppsc.200601009.

[8] U. Kuila, M. Prasad, Specific surface area and pore-size distribution in clays and shales, Geophys. Prospect. 61 (2013) 341–362, http://dx.doi.org/10.1111/1365-2478.12028.

[9] M. MahdiLabani, R. Rezaee, A. Saeedi, A.A. Hinai, Evaluation of pore size spectrum of gas shale reservoirs using low pressure nitrogen adsorption, gas expansion and mercury porosimetry: a case study from the perth and canning Basins, Western Australia, J. Petroleum Sci. Eng. 112 (2013) 7–16. http://dx.doi.org/10.1016/j.petrol.2013.11.022.

[10] M. Mastalerz, L. He, Y.B. Melnichenko, J.A. Rupp, Porosity of coal and Shale: Insights from Gas adsorption and SANS/USANS techniques, Energy Fuels 26 (2012) 5109–5120, http://dx.doi.org/10.1021/ef300735t.

[11] D.J.K. Ross, R.M. Bustin, The importance of shale composition and pore structure upon gas storage potential of shale gas reservoirs, Mar. Petroleum Geol. 26 (2009) 916–927, http://dx.doi.org/10.1016/j.marpetgeo.2008.06.004.

[12] M. Schmitt, C.P. Fernandes, J.A.B.C. Neto, F.G. Wolf, V.S.S. Santos, Characterization of pore systems in seal rocks using nitrogen gas adsorption combined with mercury injection capillary pressure techniques, Mar. Petroleum Geol. 39 (2013) 138–149. http://dx.doi.org/10.1016/j.marpetgeo.2012.09.001.

[13] H. Tian, L. Pan, X. Xiao, R.W.T. Wilkins, Z. Meng, B. Huang, A preliminary study on the pore characterization of lower silurian black shales in the chuandong thrust fold belt, southwestern China using low pressure N2 adsorption and FE-SEM methods, Mar. Petroleum Geol. 48 (2013) 8–19. http://dx.doi.org/10.1016/j.marpetgeo.2013.07.008.

[14] B. Bai, M. Elgmati, H. Zhang, M. Wei, Rock characterization of Fayetteville shale gas plays, Fuel 105 (2013) 645–652. http://dx.doi.org/10.1016/j.fuel.2012.09.043.

[15] M.E. Curtis, C.H. Sondergeld, R.J. Ambrose, C.S. Rai, Microstructural investigation of gas shales in two and three dimensions using nanometer-scale resolution imaging, AAPG Bull. 96 (4) (2012) 665–677, http://dx.doi.org/10.1306/08151110188.

[16] N.S. Fishman, P.C. Hackley, H.A. Lowers, R.J. Hill, S.O. Egenhoff, D.D. Eberl, A.E. Blum, The nature of porosity in organic-rich mudstones of the Upper Jurassic Kimmeridge Clay Formation, North Sea, offshore United Kingdom, Int. J. Coal Geol. 103 (2012) 32–50. http://dx.doi.org/10.1016/j.coal.2012.07.012.

[17] K.L. Milliken, M. Rudnicki, D.N. Awwiller, T. Zhang, Organic matter–hosted pore system, Marcellus formation (Devonian), Pennsylvania, AAPG Bull. 97 (2) (2013) 177–200, http://dx.doi.org/10.1306/07231212048.

[18] M. Josh, L. Esteban, C.D. Piane, J. Sarout, D.N. Dewhurst, M.B. Clennell, Laboratory characterisation of shale properties, J. Petroleum Sci. Eng. 88–89 (2012) 107–124, http://dx.doi.org/10.1016/j.petrol.2012.01.023.

[19] C. Zou, D. Dong, S. Wang, J. Li, X. Li, Y. Wang, D. Li, K. Cheng, Geological characteristics and resource potential of shale gas in China, Petroleum Explor. Dev. 37 (6) (2010) 641–653, http://dx.doi.org/10.1016/S1876-3804(11)60001-3.

[20] D.M. Jarvie, R.J. Hill, T.E. Ruble, R.M. Pollastro, Unconventional shale-gas systems: the mississippian barnett shale of north-central Texas as one model for thermogenic shale-gas assessment, AAPG Bull. 91 (4) (2007) 475–499, http://dx.doi.org/10.1306/12190606068.

[21] F. Hao, H. Zou, Y. Lu, Mechanisms of shale gas storage: Implications for shale gas exploration in China, AAPG Bull. 97 (8) (2013) 1325–1346, http://dx.doi.org/10.1306/02141312091.
[22] S. Chen, Y. Zhu, H. Wang, H. Liu, W. Wei, J. Fang, Shale gas reservoir characterisation: a typical case in the southern Sichuan Basin of China, Energy 36 (11) (2011) 6609–6616, http://dx.doi.org/10.1016/j.energy.2011.09.001.
[23] K. Jiao, S. Yao, C. Liu, Y. Gao, H. Wu, M. Li, Z. Tang, The characterization and quantitative analysis of nanopores in unconventional gas reservoirs utilizing FESEM-FIB and image processing: an example from the lower Silurian longmaxi Shale, upper Yangtze region, China, Int. J. Coal Geol. 128–129 (2014) 1–11. http://dx.doi.org/10.1016/j.coal.2014.03.004.
[24] J. Tan, B. Horsfield, R. Fink, B. Krooss, H. Schulz, E. Rybacki, J. Zhang, C.J. Boreham, G. van Graas, B.A. Tocher, Shale gas potential of the major marine shale formations in the upper yangtze platform, South China, Part III: mineralogical, lithofacial, petrophysical, and rock mechanical properties, Energy Fuels 28 (2014) 2322–2342, http://dx.doi.org/10.1021/ef4022703.
[25] K. Lu, X. Zhu, J. Qi, Petroleum-bearing Basin Analysis, China University of Petroleum Press, Beijing, 2006, 424pp. (in Chinese).
[26] G. Zhai, J. Song, J. Jin, W. Gao, Plate Tectonic Evolution and Formation and Evaluation of Petroleum-bearing Basins, Petroleum Industry Press, Beijing, 2002, p. 461 (in Chinese).
[27] W. Su, W.D. Huff, F.R. Ettensohn, X. Liu, J. Zhang, Z. Li, K-bentonite, black-shale and flysch successions at the Ordovician-Silurian transition, South China: possible sedimentary responses to the accretion of cathaysia to the Yangtze Block and its implications for the evolution of Gondwana, Gondwana Res. 15 (2009) 111–130, http://dx.doi.org/10.1016/j.gr.2008.06.004.
[28] C.R. Scotese, W.S. Mckerrow, Revised World Maps and Introduction, Geological Society, London 12, 1990, pp. 1–21, http://dx.doi.org/10.1144/GSL.MEM, 012.01.01.
[29] A. Delabroye, M. Vecoli, The end-Ordovician glaciation and the hirnantian stage: a global review and questions about late ordovician event stratigraphy, Earth Sci. Rev. 98 (2010) 269–282, http://dx.doi.org/10.1016/j.earscirev.2009.10.010.
[30] X. Wang, X. Chen, C. Wang, Z. Li, Ordovician to the lowest silurian chronostratigraphic subdivision in China, J. Stratigr. 28 (1) (2004) 1–17, http://dx.doi.org/10.3969/j.issn.0253-4959.2004.01.001.
[31] T. Guo, H. Zhang, Formation and enrichment mode of Jiaoshiba shale gas field, Sichuan Basin, Petroleum Explor. Dev. 41 (1) (2014) 28–36 (in Chinese with English abstract) http://www.cnki.net/kcms/doi/10.11698/PED.2014.01.03.html.
[32] Y. Ma, J. Feng, Z. Mu, P. Zhao, S. Bao, F. Wang, The potential and exploring progress of unconventional hydrocarbon resources in SINOPEC, Eng. Sci. 14 (2012) 2–29, http://dx.doi.org/10.3969/j.issn.1009-1742.2012.06.004 (in Chinese with English abstract).
[33] Z. Feng, Y. Peng, Z. Jin, P. Jiang, Z. Bao, Z. Luo, T. Ju, H. Tian, H. Wang, Lithofacies palaeogeography of the middle and late ordovician in south China, J. Palaeogeogr. 3 (4) (2001) 10–24, http://dx.doi.org/10.3969/j.issn.1671-1505.2001.04.002 (in Chinese with English abstract).
[34] J. Schoenherr, R. Littke, J.L. Urai, P.A. Kukla, Z. Rawahi, Polyphase thermal evolution in the infra-cambrian ara group (South Oman Salt Basin) as deduced by maturity of solid reservoir bitumen, Org. Geochem. 38 (2006) 1293–1318. http://dx.doi.org/10.1016/j.orggeochem.2007.03.010.
[35] G.R.L. Chalmers, R.M. Bustin, The organic matter distribution and methane capacity of the lower cretaceous strata of Northeastern British Columbia, Canada, Int. J. Coal Geol. 70 (2007), 223–339, http://dx.doi.org/10.1016/j.coal.2006.05.001.
[36] E.W. Washburn, Note on a method of determining the distribution of pore sizes in a porous material, Proceeding Natl. Acad. Sci. 7 (4) (1921) 115–116. PMCID: PMC1084764.
[37] K.S. Sing, D.H. Everett, R.A.W. Haul, L. Moscou, R.A. Pierotti, J. Rouquerol, T. Siemieniewsha, Reporting physisorption data for gas/solid systems with special reference to the determination of surface area and porosity, Pure Appl. Chem. 57 (1985) 603–619. http://dx.doi.org/10.1351/pac198557040603.
[38] J. Rouquerol, P. Llewellyn, F. Rouquerol, Is the BET equation applicable to microporous adsorbents? Stud. Surf. Sci. Catal. 160 (2007) 49–56, http://dx.doi.org/10.1016/S0167-2991(07)80008-5.
[39] J.H. de Boer, B.C. Lippens, B.G. Linsen, J.C.P. Broekhoff, A. van den Heuvel, Th. J. Osinga, The t-curve of multimolecular N2-adsorption, J. Colloid Interface Sci. 21 (4) (1966) 405–414, http://dx.doi.org/10.1016/0095-8522(66)90006-7.
[40] S. Bernard, B. Horsfield, H.M. Schulz, R. Wirth, A. Schreiber, N. Sherwood, Geochemical evolution of organic-rich shales with increasing maturity: a STXM and TEM study of the posidonia Shale (Lower Toarcian, northern Germany), Mar. Petroleum Geol. 31 (2012) 70–89, http://dx.doi.org/10.1016/j.marpetgeo.2011.05.010.
[41] G.R.L. Chalmers, D.J.K. Ross, R.M. Bustin, Geological controls on matrix permeability of devonian gas Shales in the Horn River and liard basins, northeastern British Columbia, Canada, Int. J. Coal Geol. 103 (2012b) 120–131, http://dx.doi.org/10.1016/j.coal.2012.05.006.
[42] R.G. Loucks, R.M. Reed, S.C. Ruppel, U. Hammes, Spectrum of pore types and networks in mudrocks and a descriptive classification for matrix-related mudrock pores, AAPG Bull. 96 (6) (2012) 1071–1098, http://dx.doi.org/10.1306/08171111061.
[43] R.M. Slatt, N.R. O'Brien, Pore types in the Barnett and woodford gas shales: contribution to understanding gas storage and migration pathways in fine-grained rocks, AAPG Bull. 95 (12) (2011) 2017–2030, http://dx.doi.org/10.1306/03301110145.
[44] J.C. Groen, L.A.A. Peffer, J. Pérez-Ramırez, Pore size determination in modified micro-and mesoporous materials. Pitfalls and limitations in gas adsorption data analysis, Microporous Mesoporous Mater. 60 (1–3) (2003) 1–17, http://dx.doi.org/10.1016/S1387-1811(03)00339-1.
[45] B.P. Tissot, D.H. Welte, Petroleum Formation and Occurrence: Second Revised and Enlarged Edition, Springer-Verlag, Berlin, Germany, 1984, p. 699.
[46] O. Kwon, A.K. Kronenberg, A.F. Gangi, B. Johnson, B.E. Herbert, Permeability of illite-bearing shale: 1. Anisotropy and effects of clay content and loading, J. Geophys. Res. 109 (B10205) (2004) 19, http://dx.doi.org/10.1029/2004JB003052.
[47] J.B. Curtis, Fractured shale-gas systems, AAPG Bull. 86 (11) (2002) 1921–1938, http://dx.doi.org/10.1306/61EEDDBE-173E-11D7-8645000102C1865D.
[48] G. Nichols, Sedimentology and Stratigraphy, 2nd ed., John Wiley & Sons Ltd., Oxford, UK, 2009, p. 419.
[49] T. Wan, The Tectonics of China: Data, Maps and Evolution, Higher Education Press & Berlin Heidelberg: Springer-Verlag, Beijing, 2012, 493pp.
[50] G. Pan, Q. Xiao, S. Liu, J. Den, Y. Feng, K. Zhang, Z. Zhang, F. Wang, G. Xing, G. Hao, Y. Feng, Subdivision of tectonic units in China, Geol. China 36 (1) (2009) 1–28, http://dx.doi.org/10.3969/j.issn.1000-3657.2009.01.001 (in Chinese with English abstract).
[51] X. Zeng, S. Liu, W. Huang, C. Zhang, Comparison of silurian longmaxi formation shale of sichuan Basin in China and carboniferous barnett formation shale of Fort Worth Basin in United States, Geol. Bull. China 30 (2/3) (2011) 372–384, http://dx.doi.org/10.3969/j.issn.1671-2552.2011.02.024 (in Chinese with English abstract).
[52] J.D. Arthur, B. Langhus, D. Alleman, An Overview of Modern Shale Gas Development in the United States, ALL Consulting, 21pp., 2008 http://www.all-llc.com/publicdownloads/ALLShaleOverviewFINAL.pdf.